



HAL
open science

Airborne observations of bioaerosol over the Southeast United States using a Wideband Integrated Bioaerosol Sensor

Luke D. Ziemba, Andreas J. Beyersdorf, Gao Chen, Chelsea A. Corr, Suzanne N. Crumeyrolle, Glenn Diskin, Charlie Hudgins, Robert Martin, Tomas Mikoviny, Richard Moore, et al.

► To cite this version:

Luke D. Ziemba, Andreas J. Beyersdorf, Gao Chen, Chelsea A. Corr, Suzanne N. Crumeyrolle, et al.. Airborne observations of bioaerosol over the Southeast United States using a Wideband Integrated Bioaerosol Sensor. *Journal of Geophysical Research: Atmospheres*, 2016, 121, pp.8506-8524. 10.1002/2015JD024669 . insu-03686195

HAL Id: insu-03686195

<https://insu.hal.science/insu-03686195>

Submitted on 2 Jun 2022

HAL is a multi-disciplinary open access archive for the deposit and dissemination of scientific research documents, whether they are published or not. The documents may come from teaching and research institutions in France or abroad, or from public or private research centers.

L'archive ouverte pluridisciplinaire **HAL**, est destinée au dépôt et à la diffusion de documents scientifiques de niveau recherche, publiés ou non, émanant des établissements d'enseignement et de recherche français ou étrangers, des laboratoires publics ou privés.

Copyright

RESEARCH ARTICLE

10.1002/2015JD024669

Special Section:

Studies of Emissions and Atmospheric Composition, Clouds and Climate Coupling by Regional Surveys, 2013 (SEAC4RS)

Key Points:

- The southeast USA region is a significant source of bioaerosols
- Shallow convection allows vertical transport of bioaerosols
- Emission rates from different land types are relatively homogeneous

Correspondence to:

L. D. Ziemba,
luke.ziemba@nasa.gov

Citation:

Ziemba, L. D., et al. (2016), Airborne observations of bioaerosol over the Southeast United States using a Wideband Integrated Bioaerosol Sensor, *J. Geophys. Res. Atmos.*, 121, 8506–8524, doi:10.1002/2015JD024669.

Received 17 DEC 2015

Accepted 1 JUN 2016

Accepted article online 4 JUN 2016

Published online 21 JUL 2016

Published 2016. This article is a U.S. Government work and is in the public domain in the USA.

Airborne observations of bioaerosol over the Southeast United States using a Wideband Integrated Bioaerosol Sensor

Luke D. Ziemba¹, Andreas J. Beyersdorf¹, Gao Chen¹, Chelsea A. Corr^{1,2}, Suzanne N. Crumeyrolle^{2,3}, Glenn Diskin¹, Charlie Hudgins^{1,4}, Robert Martin¹, Tomas Mikoviny⁵, Richard Moore¹, Michael Shook^{1,4}, K. Lee Thornhill^{1,4}, Edward L. Winstead^{1,4}, Armin Wisthaler^{5,6}, and Bruce E. Anderson¹

¹NASA Langley Research Center, Hampton, Virginia, USA, ²Universities Space Research Association, Columbia, Maryland, USA, ³Laboratoire d'Optique Atmosphérique, CNRS-Université de Lille, Villeneuve d'Ascq, France, ⁴Science Systems and Applications, Inc., Lanham, Maryland, USA, ⁵Institute of Ion Physics and Applied Physics, University of Innsbruck, Innsbruck, Austria, ⁶Department of Chemistry, University of Oslo, Oslo, Norway

Abstract Biological aerosols represent a diverse subset of particulate matter that is emitted directly to the atmosphere in the form of (but not limited to) bacteria, fungal spores, pollens, viruses, and plant debris. These particles can have local air quality implications, but potentially play a larger climate role by acting as efficient ice nucleating particles (INPs) and cloud condensation nuclei. We have deployed a Wideband Integrated Bioaerosol Sensor on the NASA DC-8 aircraft to (1) quantify boundary layer (BL) variability of fluorescent biological aerosol particle (FBAP) concentrations in the Southeast United States (SEUS), (2) link this variability explicitly to land cover heterogeneity in the region, and (3) examine the vertical profile of bioaerosols in the context of convective vertical redistribution. Flight-averaged FBAP concentrations ranged between 0.1 and 0.43 scm^{-3} (cm^{-3} at standard temperature and pressure) with relatively homogeneous concentrations throughout the region; croplands showed the highest concentrations in the BL (0.37 scm^{-3}), and lowest concentrations were associated with evergreen forests (0.24 scm^{-3}). Observed FBAP concentrations are in generally good agreement with model parameterized emission rates for bacteria, and discrepancies are likely the result of fungal spore contributions. Shallow convection in the region is shown to be a relatively efficient lofting mechanism as the vertical transport efficiency of FBAP is at least equal to black carbon aerosol, suggesting that ground-level FBAP survives transport into the free troposphere to be available for INP activation. Comparison of the fraction of coarse-mode particles that were biological (f_{FBAP}) suggested that the SEUS ($f_{\text{FBAP}} = 8.5\%$) was a much stronger source of bioaerosols than long-range transport during a Saharan Air Layer (SAL) dust event ($f_{\text{FBAP}} = 0.17\%$) or summertime marine emissions in the Gulf of Mexico ($f_{\text{FBAP}} = 0.73\%$).

1. Introduction

The aerosol indirect effect remains one of the most uncertain aspects of Earth's climate system. In particular, heterogeneous freezing (i.e., the role of aerosols as ice nucleating particles (INPs)) mechanisms are poorly understood both mechanistically [Ervens et al., 2011] and because of sparse ambient measurements, even in the wake of ongoing scientific focus and instrument development [DeMott et al., 2011]. Parameterizations of INPs based on ambient temperature and coarse-mode (with diameter greater than 0.5 μm) aerosol number concentrations have moved the field forward [DeMott et al., 2010] but lack a predictive means of incorporating more complex microphysical and chemical constraints. Improved representation of INPs using ambient observations will contribute to more accurate assessment of aerosol indirect climate effects.

Laboratory studies have historically been drawn toward a subset of biologically derived coarse-mode aerosols as efficient INPs under very controlled conditions [Hoose and Mohler, 2012], with the implication that they exhibit freezing onset at temperatures warmer than for mineral dust [Després et al., 2012, and references therein]. Globally, bioaerosols tend to be overlooked as relevant INPs (compared to mineral dust) because of assumed low concentrations [Jaenicke, 2005], an inference that is based on a severe lack of in situ observations. Bacterial cells and fungal spores are thought to dominate the biological number concentration, but global modeling suggests that these particles only have a minor effect on ice formation and precipitation rates [Sesartic et al., 2012]. Still, these bioaerosols may be important at warmer cloud temperatures and at regional scales [Hoose et al., 2010; Spracklen and Heald, 2014]. Current model emissions constraints typically

rely on ground-based manual counting techniques and bacterial cultures [Burrows *et al.*, 2009a, 2009b], methods that are intrinsically uncertain and have suboptimal time response. Thus, more comprehensive in situ observations are needed to validate bioaerosol global budgets [Heald and Spracklen, 2009] and to accurately assess climatological effects.

Airborne single-particle mass spectroscopic techniques have been applied recently not only to provide a direct link between long-range transport of biological aerosols and induced precipitation in the western U.S. [Pratt *et al.*, 2009; Creamean *et al.*, 2013] but also to discount the role of biological aerosols in cirrus formation near the midlatitude tropopause [Cziczo *et al.*, 2013]. Tobo *et al.* [2013] showed a direct relationship between biological aerosols and INPs from ground-based measurements with the unique continuous flow diffusion chamber technique, resulting in an amendment to the DeMott *et al.* [2010] parameterization incorporating a chemically specific fraction that autofluoresces (i.e., the fluorescent biological aerosol particle (FBAP) concentration). Fluorescence techniques to quantify bioaerosols in the ambient atmosphere are now being more widely used [e.g., Gabey *et al.*, 2010; Pan *et al.*, 2011; Huffman *et al.*, 2010].

Fluorescence detection of bioaerosols is often advantageous because of specificity for complex organic compounds like proteins and enzymes, with an insensitivity to mineral dust. Single-wavelength fluorescence detection is utilized by the UV Aerodynamic Particle Sizer (TSI, Inc.) and at two wavelengths for the Wideband Integrated Bioaerosol Sensor (WIBS-4A, Droplet Measurement Technologies, Boulder, CO); both instruments are commercially available. Coupled with a size detection scheme, each of these techniques provides a powerful tool used to characterize coarse-mode aerosol and quantify the mixing state of particles that contain biological material. Interferants to fluorescence detection exist, and nonbiological materials have been shown to induce fluorescence but with intensities that are generally too weak (e.g., for mineral dusts, dry humic, or fulvic acids) or the fluorophores are found on particles smaller than the WIBS detection region (e.g., polycyclic aromatic hydrocarbons associated with soot) [Pöhlker *et al.*, 2012].

Results presented here utilize a WIBS-4A instrument for airborne FBAP observations. Vertical profiling provides simultaneous insight into ground-level emissions, venting of boundary layer (BL) constituents into a transition/cloud layer, and transport into the free troposphere (FT) by storm-related strong convection. Dust and bioaerosols have been inferred to travel long distances, e.g., Prospero *et al.* [2005], and Hallar *et al.* [2011], and the vertical profile of bioaerosols over the Southeast United States (SEUS) helps elucidate different transport mechanisms. The SEUS region contains a mixture of natural and agricultural land use types, contains areas of strong biogenic emissions, and is noted for frequent convective storms. Transport of coarse-mode aerosols out of the BL is particularly important for constraining the upper tropospheric concentration of INP-efficient biological aerosols and for assessing aerosol indirect effects.

The WIBS-4A instrument has been modified for operation aboard the NASA DC-8 aircraft and deployed during the NASA SEAC⁴RS (Studies of Emissions and Atmospheric Composition, Clouds, and Climate Coupling by Regional Surveys) campaign. Data collected during flights in August–September 2013 are used to assess the horizontal and vertical variability of bioaerosol concentrations, mixing state, and size distribution in the SEUS region. Specifically, we relate differences in fluorescence characteristics of biological aerosol with the distribution of land cover, highlighting the WIBS-4A capability to effectively segregate forest and agricultural emissions. Additionally, SEUS vertical profiles evaluate FBAP transport out of the continental BL. Observations in the SEUS are contrasted with measurements over the clean Gulf of Mexico, in the western U.S., and of a Saharan Air Layer (SAL) dust outbreak to highlight the importance of bioaerosol emissions from this complex region.

2. Methods

2.1. SEAC⁴RS Flights

Twenty-one science flights were completed during SEAC⁴RS (Figure 1) based at Ellington Field in Houston, TX. Twelve of these flights were dedicated to sampling the SEUS region (Figure 1, inset). The SEUS region was defined here by a latitude greater than 30.2°N and less than 38.6°N and a longitude greater than 265.5°E and less than 279.8°E. Forty-four percent (27,130 10 s data points) of the SEAC⁴RS data set is inside the SEUS domain, the remainder is excluded from this analysis except profiling data used for comparison.

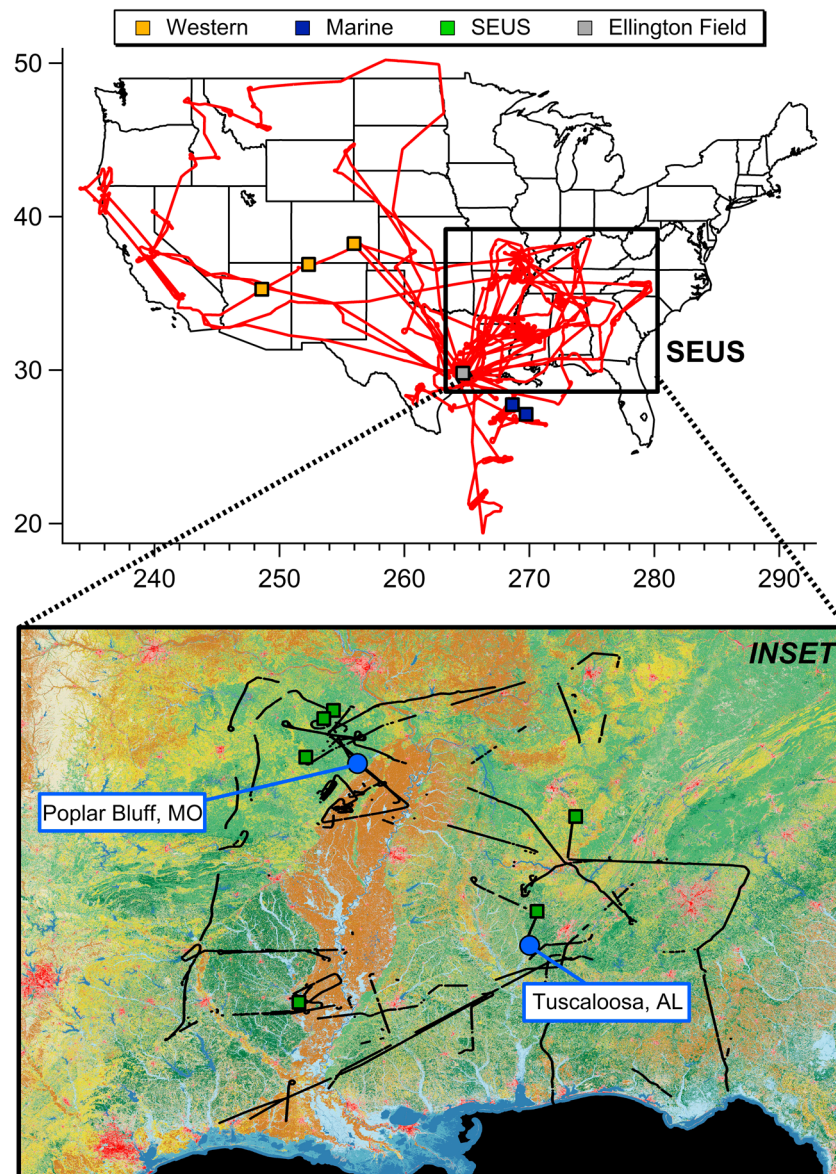


Figure 1. SEAC⁴RS flight tracks (red) and profile locations (squares). The targeted SEUS region is shown in the inset (bottom), with black lines representing low-altitude flight tracks. NLCD2011 land cover types are colored as follows in the inset: Developed land (red), evergreen forest (dark green), deciduous forest (light green), shrubs and grasslands (tan), pastures (yellow), cultivated crops (brown), and wetlands and open water (blue). Ground sites used for meteorological context in Figure 5 are shown as circles in the inset: Poplar Bluff, MO and Tuscaloosa, AL.

Locations with vertical profiles, defined as a monotonic descent or ascent (either spiraling or inline) covering at least 8 km altitude and lasting no more than 25 min (i.e., a minimum ascent/descent rate of 300 m min⁻¹), are also shown in Figure 1 for western and marine regions. Six SEUS profiles are also noted in the inset. Much of the SEUS sampling was done at low altitude (less than 1 km), with fairly even spatial coverage sampling a range of different land use types in the region.

2.2. WIBS-4A Airborne Operation

The WIBS-4A (referred to henceforth as “WIBS”) was operated on board the NASA DC-8 aircraft in conjunction with the LARGE (Langley Aerosol Research Group Experiment, <http://science.larc.nasa.gov/large>) aerosol payload, consisting of a suite of instruments to measure aerosol microphysical, chemical, and optical properties. Ambient air was introduced isokinetically into the aircraft through a shrouded solid diffuser inlet [Clarke et al., 2004] with

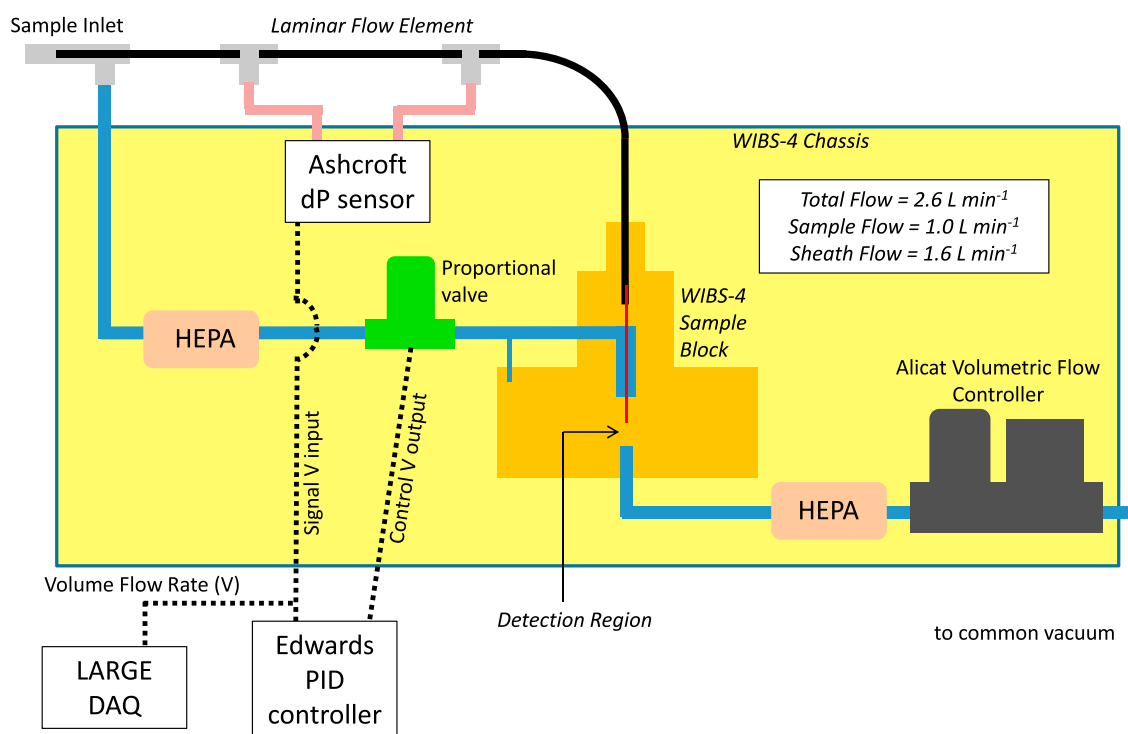


Figure 2. Schematic of updated flow control system for the WIBS.

a 50% transmission cutoff of $5.0\ \mu\text{m}$ aerodynamic diameter [McNaughton *et al.*, 2007]. Thus, the WIBS here measures particles between 0.6 and $5.0\ \mu\text{m}$ diameter. WIBS flow was immediately split at a custom-designed sampling manifold (Brechtel Manufacturing, Inc., Hayward, CA) and delivered to the instrument through approximately $1.5\ \text{m}$ of nominally $8\ \text{mm}$ inner-diameter conductive silicone tubing (residence time of $1.7\ \text{s}$). Tubing between the inlet and instrument contained four 90° bends that resulted in cumulative theoretical transmission efficiencies of 0.998 , 0.900 , and 0.741 for $1\ \mu\text{m}$, $3\ \mu\text{m}$, and $5\ \mu\text{m}$ diameter particles, respectively. Losses due to gravitational settling are more difficult to assess but are estimated to be on the order of 10% for $3\ \mu\text{m}$ particles. While particle losses become more significant at $5\ \mu\text{m}$ diameter due to the combination of limited inlet transmission and transport tubing losses, the peak in FBAP size at $2\text{--}3\ \mu\text{m}$ diameter is relatively efficiently sampled. Still, due to calculation uncertainties we have chosen not to correct the data for these losses.

The factory-delivered flow control system for the WIBS was modified to allow sampling from an airborne platform, especially to compensate for fast changes in ambient pressure and to allow recording of flow rates for postprocessing and data quality control; a schematic is shown in Figure 2. A common vacuum source is provided by the LARGE suite and is controlled to a constant total WIBS flow rate of $2.6\ \text{L min}^{-1}$. This flow is split into a sheath flow and sample flow. A proportional valve (MKS, model 0248A-12044, $50\ \text{L min}^{-1}$ range) was installed in the sheath line (replacing a passive orifice) which allowed for active control (Edwards, model 1501B process controller) of the sample flow entering the system to a constant $1.0\ \text{L min}^{-1}$ measured by a custom-designed laminar flow element (LFE, with an Ashcroft model RXLdp differential pressure transducer). The LFE was calibrated prior to deployment and operates effectively over a range of $0.2\text{--}1.4\ \text{L min}^{-1}$. This improved sample delivery system ensures that a constant sample air velocity is maintained in the WIBS sampling region to preserve timing of the size/fluorescence detection technique over the full altitude range of the DC-8 aircraft.

The detection scheme of the WIBS has been detailed elsewhere [Kaye *et al.*, 2000, 2005; Gabey *et al.*, 2010] and is only briefly described here. Particles are initially sized using the 90° side-scattering signal from a $635\ \text{nm}$ continuous-wave diode laser. The scattering intensity is directly related to particle diameter and was calibrated prior to deployment using a range of National Institute of Standards and Technology traceable polystyrene latex spheres (PSLs with 0.8 , 0.9 , 1.0 , 1.3 , 2.0 , and $3.0\ \mu\text{m}$ diameter, Thermo Scientific Inc.). Thus, all WIBS sizing is optically referenced to a PSL material refractive index of 1.59 . WIBS size distributions agreed well with a

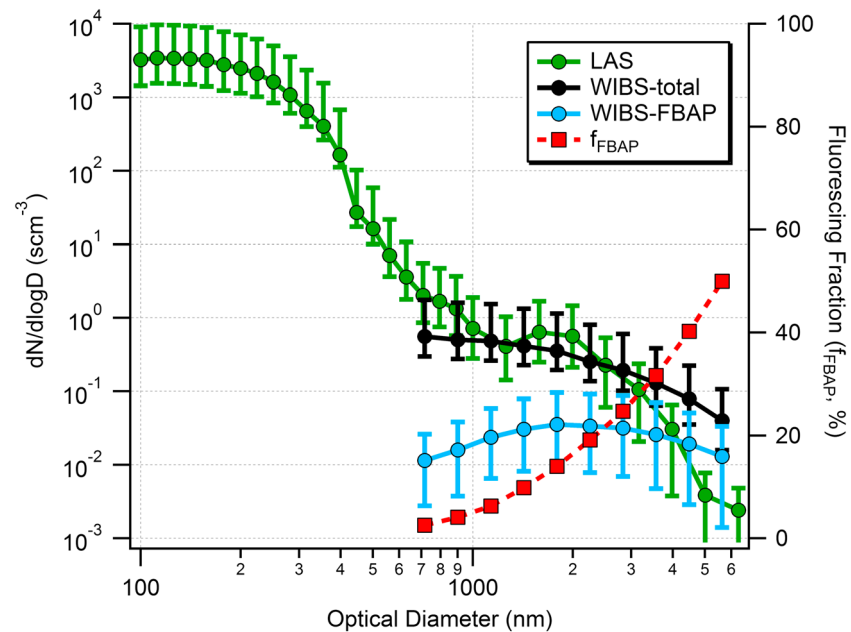


Figure 3. Particle size distributions for all low-altitude, nonbiomass burning aerosol measured by the LAS (green) and WIBS (black). The campaign-averaged FBAP (blue) size distribution is also shown. Error bars represent the average value ± 1 geometric standard deviation at each size step.

similarly calibrated laser aerosol spectrometer (LAS, TSI, Inc.) as shown in Figure 3. The comparison deviates at diameters greater than $4 \mu\text{m}$, likely attributed to the difficulty of transporting coarse-mode aerosol to each independent instrument.

Each single-particle event observed by the WIBS exceeding $0.6 \mu\text{m}$ diameter is followed by successive 280 nm and 370 nm xenon flashtube pulses. Particles smaller than $0.6 \mu\text{m}$ diameter do not produce a scattering intensity large enough to be detected and thus do not trigger a fluorescence measurement. Fluorescence intensity from the 280 nm excitation wavelength is based on detection of the amino acid tryptophan, while the 370 nm excitation wavelength is based on detection of the coenzyme nicotinamide adenine dinucleotide [Gabey *et al.*, 2010]. Two broadband detectors at 310–400 and 420–650 nm measure fluorescence from each of the successive excitation wavelength pulses, where the following detection definitions are employed based on Perring *et al.* [2015]: Type A = 280 nm excitation on the 310–400 nm detector only, Type B = 280 nm excitation on the 420–650 nm detector only, and Type C = 370 nm excitation on the 420–650 nm detector only. Signal from 370 nm excitation is saturated on the 310–400 nm detector by direct scattering and is not recorded. Particles that exhibit coincident fluorescence in more than one channel are labeled accordingly (i.e., Type AB particles fluorescence from 280 nm excitation on both the 310–400 nm and 420–650 nm detectors). Particles which fluoresce in all three channels simultaneously are labeled as Type ABC and quantified as FBAP, and thus all references to number concentrations or fractions of fluorescing particles (N_{FBAP}) refer to particles that fluoresce in all three WIBS channels. Nonfluorescing particles are defined as particles that did not fluoresce in any of the three WIBS channels.

Size distributions comparing FBAP and nonfluorescing particles are shown in Figure 4 for upper (a), middle (b), and lower troposphere (c) sampling. Distributions are averages of single-particle events for 10 constant-dlogD bins from 0.6 to $6.0 \mu\text{m}$ optical diameter. Through the full altitude range, FBAP size distributions are easily distinguishable from nonfluorescing particles due to a peak in $dN/d\log D$ from 1 to $3 \mu\text{m}$ diameter. FBAP particles were observed at low altitude with a geometric mode at $2.1 \mu\text{m}$. A reduction in geometric mode to $1.5 \mu\text{m}$ was observed for middle and upper tropospheric sampling (Figure 4). Since the theoretical inlet sampling efficiency decreases from a 50% cutoff of $5.0 \mu\text{m}$ at the surface to $3.2 \mu\text{m}$ at 12 km [McNaughton *et al.*, 2007], this difference is at least partially attributed to sampling artifact. Still, it is obvious that the FBAP size distribution differs from nonfluorescing particles as nonfluorescing size distributions had monotonically decreasing concentrations with size, peaking at submicron diameters outside of the WIBS detection region (i.e., LAS distributions

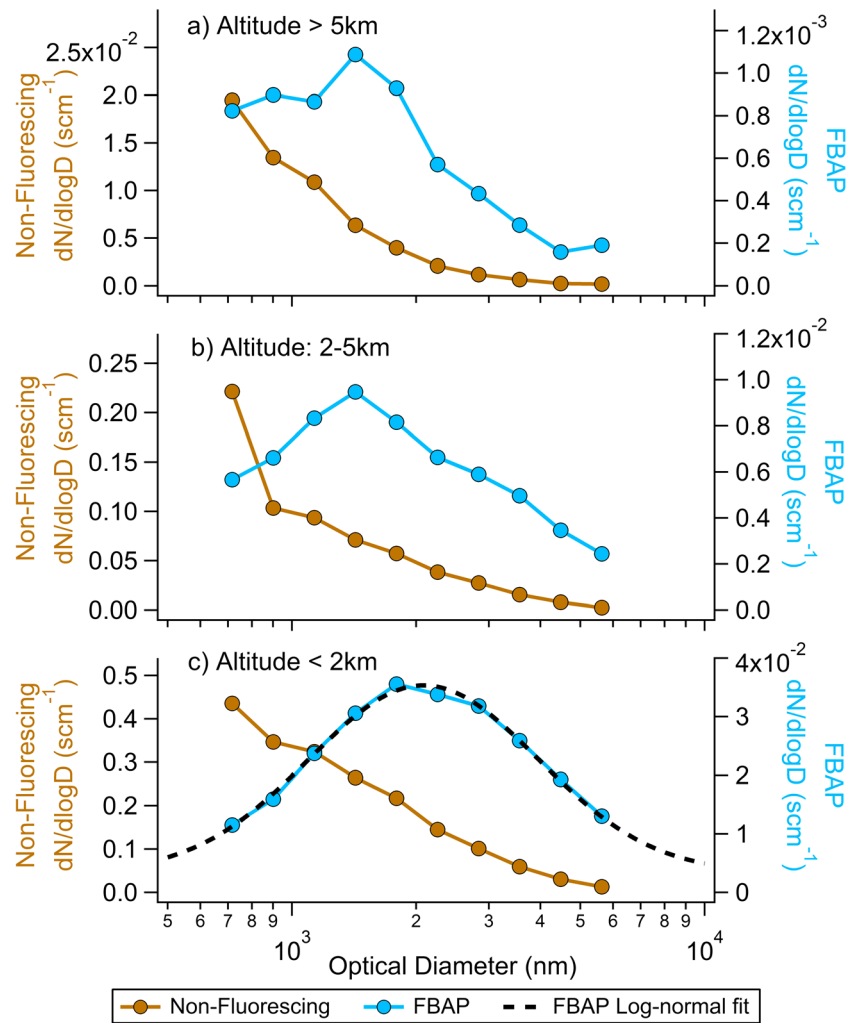


Figure 4. FBAP (right axes) and nonfluorescing (left axes) aerosol size distributions for the full campaign in the SEUS region for (a) upper troposphere, (b) middle troposphere, and (c) lower troposphere sampling, including a lognormal FBAP fit in the lower troposphere. Note that y axis scaling is optimized to illustrate each distribution shape.

indicate a peak at less than 200 nm diameter in Figure 3). All low-altitude fluorescing particles, especially Type A, Type B, and Type BC showed qualitatively similar size distributions to FBAP peaking at supermicron diameter. The fraction of coarse-mode aerosols identified as FBAP increases with size, from 5% at 1.0 μm to 50% at 6.0 μm diameter (Figure 3).

At low altitude, a lognormal fit describes the FBAP distribution well

$$0.0034 + 0.032 \cdot \text{EXP} \left[- \left(\ln \left(\frac{X/2085}{0.90} \right) \right)^2 \right] \quad (1)$$

where X is the particle diameter in nm. Based on extrapolation of this fit, only 13.8% of the FBAP number concentration lies outside of the WIBS detection window (the upper limit is actually governed here by the aircraft inlet, not the WIBS technique), but due to size distribution variability data were not corrected for this potential bias. Also, note that small changes in the WIBS lower detection limit would not significantly alter calculated FBAP number concentrations, i.e., a quantification scheme using a 1.0 μm threshold instead of the 0.6 μm threshold used here, as in *Perring et al. [2015]*, results in a decrease in concentration by 6%.

2.2.1. WIBS “Forced-Triggering” (FT) Mode

To ensure instrument noise does not manifest as falsely identified fluorescent particles, intensity thresholds are determined once prior to each flight. The xenon lamp detection scheme is operated for particle-free air to

assess this background variability in classifying fluorescent particles. With no air flow, the system is periodically triggered and the three-channel fluorescence from 500 excitation flash events is recorded. Fluorescence intensity thresholds are determined as the average intensity plus 2.5 standard deviations [Gabey *et al.*, 2010].

While the intensity of FT signals on each detector is used to remove system noise and prevent false-positive counting, the percent of FT data points exceeding that threshold is used to quantify the detection limit for fluorescing-fraction (f) values. For reference, average threshold values (in arbitrary units) used for this study were 93.8, 69.1, and 9.8 for Type A, Type B, and Type C detectors, respectively. Single-channel detection with the WIBS is rather uncertain; 6.1, 1.1, and 1.5% of FT events for each type, respectively, exceeded the threshold and were falsely counted as real fluorescent particles. Conversely, only 0.06% of all FT events exceeded thresholds for all three detectors simultaneously. This is the motivation for using the three-channel (i.e., Type ABC) definition to conservatively quantify bioaerosol throughout this study, as noted above.

2.2.2. WIBS-4A Ambient Data Analysis

The following filtering criteria were used to eliminate potentially erroneous ambient data on a particle-by-particle basis.

1. Particles with diameter less than 0.6 μm are removed.
2. Particles exhibiting fluorescence intensity lower than the flight-by-flight threshold value are counted as nonfluorescing.
3. Particles are removed if sample flow rate deviated more than 5% from 1.0 L min^{-1} .

Number concentrations of fluorescent biological aerosol particles (N_{FBAP}) were calculated by (1) summing the number of single-particle events that exhibited fluorescence in all three channels (i.e., Type ABC) simultaneously for a 10 s period, (2) dividing by the measured LFE sample flow rate, and (3) correcting the air volume to standard temperature (0°C) and pressure (1013 mb). N_{FBAP} is reported in units of standard cm^{-3} (scm^{-3}). The three-channel definition is more conservative than the two-channel approach by Gabey *et al.* [2010] and was chosen because of the potential for false-counting noted above. Particles fluorescing in single channels and combinations of two channels were likely biological and are considered only in the fingerprinting analysis in section 3.3.2 but are not quantified as N_{FBAP} or f_{FBAP} .

The fraction of fluorescent particles (f_{FBAP} , expressed as a percent) is determined at 10 s resolution as the ratio of the sum fluorescing particles in all three channels to the sum of all particles counted by the WIBS (the remainder of which is primarily composed of mineral dust). Fluorescing fraction (f_{FBAP}) for other time scales is always determined by summing single-particle events and never calculated as an average of 10 s values. Note again that particles fluorescing in only one or two channels are not included as fluorescing particles in the calculation of f_{FBAP} . Lastly, 10 s averaged data satisfying any one of the following two criteria were flagged and not considered for this analysis as follows.

1. Cloud particles can produce shattering artifacts that affect in situ aerosol measurements. All data coincident with cloud penetrations have been removed based on nonzero signal from wing-mounted microphysical probes [Lawson, 2011]. In the SEUS, 14% of data were removed due to cloud contamination, 85% of which were above 1 km altitude.
2. Highly concentrated biomass burning sampling yielded significant FBAP concentrations. While it is possible that turbulence and convection associated with wildfires could loft dust and biological aerosols, polycyclic aromatic hydrocarbon condensation onto dust particles represents a potential fluorescence interference [Pöhlker *et al.*, 2012] resulting in nonbiological artifact. Thus, instances of biomass burning (1.1% of SEUS sampling) were removed from the 10 s data set using a threshold of 250 parts per trillion by volume acetonitrile.

2.3. Auxiliary Measurements and Land Cover Data

A large suite of particle and gas-phase observations were made aboard the DC-8 for SEAC⁴RS, and a subset of those measurements is considered here. Isoprene, monoterpene, acetonitrile, and toluene mixing ratios were measured by a proton-transfer reaction mass spectrometer [Müller *et al.*, 2014]. Carbon monoxide (CO) observations were made by differential absorption spectrometry [Sachse *et al.*, 1987]. Black carbon (BC) mass concentrations were measured by a single-particle soot spectrometer [Schwarz *et al.*, 2006]. Total aerosol particle number concentration measurements in Figure 3 are from a laser aerosol spectrometer (LAS, Szymanski [2002]) that has been modified for flight operation.

Table 1. Comparison of Land Cover Types Observed During SEAC⁴RS

Land Cover Type	SEUS Coverage (% of Land Area)	Model Flux ($\text{m}^{-2} \text{s}^{-1}$)	Model ^a N_{FBAP} (scm^{-1})	Observed Median N_{FBAP} (scm^{-1})
Forest	44	187	0.014–0.04	0.31 (deciduous) 0.24 (evergreen)
Crop land	13	1,578	0.11–0.34	0.37
Pasture	15	1400 ^b	NA	0.30
Grassland	3	1811	0.13–0.39	0.29
Shrub	6	619	0.04–0.13	0.23
Wetlands	8	1200 ^b	NA	0.26
Developed	7	NA	NA	NA
Open water, barren, etc	3	NA	NA	NA

^aAssuming a boundary layer height of 1.2 km with a residence time of 1–3 days.

^bNot included in *Burrows et al.* [2009a, 2009b] parameterization; calculated based on observed N_{FBAP} and assumptions used in ^a. NA=Not Applicable.

Land cover data for the SEUS were taken from the National Land Cover Database 2011 (NLCD2011) obtained from the Multiresolution Land Characteristics Consortium and derived from Landsat imagery [Jin *et al.*, 2013]. Spatial resolution for land cover data is 30 m, and each pixel is classified based on *Anderson et al.* [1976]. Brief descriptions of relevant types are as follows.

1. *Forest*: trees taller than 5 m having similar seasonal growth patterns that are segregated as “deciduous,” “evergreen,” and “mixed.”
2. *Shrubs and grasslands*: vegetation less than 5 m height.
3. *Agricultural lands*: include two types, pastures (for livestock grazing) and cultivated crops (e.g., corn, soybeans, vegetables, orchards, and vineyards)
4. *Woody wetlands*: areas where soils are periodically saturated with water.

Each 10 s SEUS data point below 1 km altitude with coinciding flight-level wind speed less than 5 m s^{-1} was labeled with the corresponding land cover type using the spatial analyst extension of ArcGIS (Environmental Systems Research Institute, Desktop version 10.2.2). The 1 km threshold was chosen based on the aggregated boundary layer height observed in the region [Wagner *et al.*, 2015]. The distribution of land use types was not significantly altered by small changes in these threshold choices. Since the land cover resolution is much finer than for 10 s aircraft sampling, the characteristic land cover for each aircraft data point was selected by (1) considering nine equally spaced pixels inside a $1.3 \times 1.3 \text{ km}$ box (based on an average airspeed of 133 m s^{-1}) centered at the DC-8 location for each 10 s data point and (2) choosing the predominant type of these nine pixels to represent the aircraft data point. Data for deciduous forest, evergreen forest, pastures, and cultivated crop regions were sampled most frequently in the SEUS (Table 1). Developed spaces, barren land, and herbaceous wetlands were identified in the NLCD2011 database but were not sampled by the aircraft with sufficient statistics to report here. Types used in this study are analogous to those used to estimate ecosystem-dependent emissions for global modeling, e.g., *Spracklen and Heald* [2014] and *Burrows et al.* [2009a, 2009b].

3. Results and Discussion

Ground-level variability in FBAP number, fraction, and fluorescence characteristics has been attributed to a combination of differences in the sampling time of day (e.g., *Crawford et al.*, [2014]), meteorological variables (e.g., precipitation from *Huffman et al.* [2013]), and land cover-driven emissions [Burrows *et al.*, 2009a, 2009b]. Variability in the vertical profile of bioaerosol properties will then depend on lofting mechanisms (i.e., convection) superimposed on these ground-level differences. These mechanisms are discussed in the following sections.

3.1. Temporal Variability: Links to Meteorological Conditions

A time series of flight-averaged N_{FBAP} is shown in Figure 5 for low-altitude sampling (less than 1 km pressure altitude, circles), along with box plot N_{FBAP} statistics for each flight. Average low-altitude N_{FBAP} ranged from 0.10 (12 August) to 0.43 scm^{-3} (11 September), with 90th percentile values up to 0.77 scm^{-3} . FBAP represents a small fraction of the total aerosol population, as SEUS accumulation mode concentrations are generally 4 orders of magnitude greater (Figure 3).

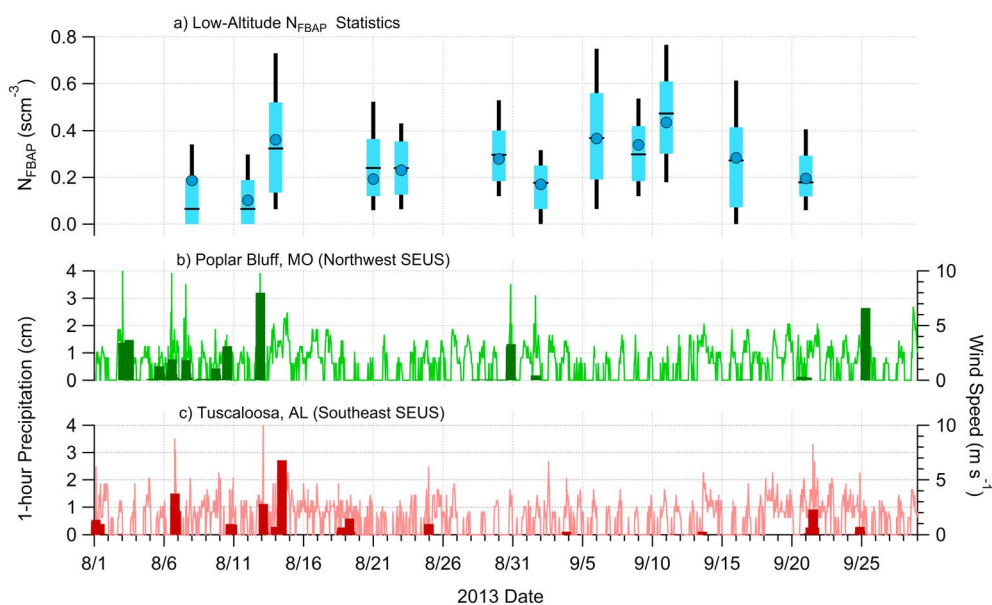


Figure 5. (a) Time series for flight-averaged N_{FBAP} statistics and meteorological parameters for (b) Poplar Bluff, MO and (c) Tuscaloosa, AL during SEAC⁴RS. For Figure 5a, circles are average values, horizontal lines are median values, the line extents are interdecile ranges (90th and 10th percentiles), and the box extents are the interquartile ranges (75th and 25th percentiles). All FBAP statistics reference low-altitude (less than 1 km pressure altitude) sampling. Dark bars (Figures 5b and 5c) are 1 h precipitation, and lines are wind speed.

Coincident ground-level wind speed and precipitation rate data are included in Figure 5 to provide a meteorological context to these observations. Data from Poplar Bluff, MO (Figure 5b) and Tuscaloosa, AL (Figure 5c) were chosen to represent the region, since these areas were frequently sampled during SEAC⁴RS (shown on the map in Figure 1). Rain events were more frequent in the SEUS in the first 16 days of August, and rain-free conditions were observed from 1 September through 20 September. This dry period had wind speeds less than 5 m s^{-1} (6 September to 11 September) and yielded the highest N_{FBAP} , contrary to a dominant wind-driven mechanical generation mechanism for coarse-mode aerosol [Jones and Harrison, 2004].

Statistically, ground-level N_{FBAP} was largest at the minimum and maximum wind speeds measured during SEAC⁴RS, with minimum concentrations observed at $4\text{--}5 \text{ m s}^{-1}$ (Figure 6a). The highest N_{FBAP} (90th percentile values) was 0.87 scm^{-3} for $9\text{--}10 \text{ m s}^{-1}$ wind speeds and 0.76 scm^{-3} for $0\text{--}1 \text{ m s}^{-1}$ wind speeds. This reinforces two controlling mechanisms for N_{FBAP} : stagnant conditions that continually feed and concentrate ground-level FBAP in the absence of wet deposition (e.g., 6 September to 11 September) and faster winds associated with rain events that stimulate higher mechanical emission rates (e.g., 14 August).

Evidence linking rain events to high bioaerosol concentrations has been shown, e.g., at the forested Manitou Experimental Forest Observatory site near Colorado Springs, CO [Huffman *et al.*, 2013]. Crawford *et al.* [2014] suggest that fungal spores may dominate the precipitation-driven FBAP production, and that bacteria are more prevalent in dry periods. Mechanisms to explain the link between bioaerosols and rainfall are likely specific to vegetative and bioaerosol type, including wet ejection of fungal spores [Huffman *et al.*, 2013]. For this study, only the 14 August case could potentially be attributed to precipitation initiation. The stagnant 6 September to 11 September period noted earlier occurred during a particularly dry period in the SEUS, meaning that high N_{FBAP} observations during this time period were certainly not the result of precipitation-induced emissions. Thus, it is unlikely that precipitation events were driving day-to-day N_{FBAP} variability in the region, although we note that our measurements refer to a limited particle size range and were collected above ground level. Statistically, no RH or surface temperature dependence was observed during the SEAC⁴RS mission (Figure 6c), in contrast to other studies linking emissions to increased RH [Jones and Harrison, 2004].

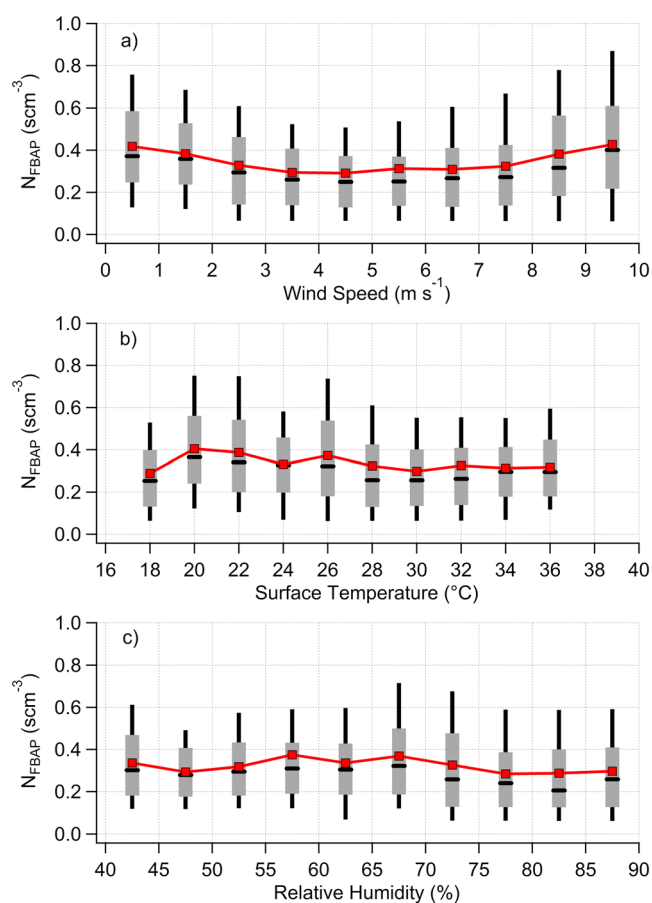


Figure 6. Binned N_{FBAP} statistics for ground-level (less than 1 km altitude) SEUS data as a function of flight-level (a) wind speed, (b) surface temperature, and (c) relative humidity. Box and whisker method is the same as Figure 5a. Red squares represent average values.

3.2. Spatial Variability: Dependence on Land Cover

To better explain low-altitude bioaerosol variability, land use in the SEUS region was considered as a factor controlling N_{FBAP} , f_{FBAP} , and observed fluorescence spectral characteristics. An ideal example of this link to land cover is shown in Figure 7 for a 6 min flight segment on 23 August when the aircraft sampled at 0.3–0.6 km altitude passing over an evergreen forest transition to crop land just west of the Mississippi River and Greenville, MS. Croplands in this region are noted for their significant production of soybeans, rice, and cotton. Winds were out of the northeast at 4.6 m s^{-1} at flight level, nearly parallel with the division between the two land use types and presumably limited mixing between the two sources. Note that types are accurately identified for individual airborne data points. It is clear that monoterpene mixing ratios are elevated and more variable over the forest while these emissions are suppressed over croplands. N_{FBAP} is relatively unchanged over this transition, but the FBAP speciation seems to change between land-covers, as indicated by higher Type A/Type B ratio values over the evergreen forest than over the cropland. Differences in the fluorescence spectra like this have

been documented previously [Pöhlker *et al.*, 2012] and indicate intrinsic differences in the fluoropore speciation associated with diverse land cover emissions.

Using the NLCD2011 for the SEUS region, gas and aerosol properties were aggregated for pertinent land cover categories and are presented in Figure 8. Each land cover category is shown as a vertical column labeled from left to right: deciduous forest, evergreen forest, shrubs, grasslands, agricultural pastures, agricultural croplands, and woody wetlands. Statistics for gas phase tracers isoprene and monoterpenes are included as a validation of the method (Figure 8, top). As expected [Guenther *et al.*, 1994], the largest isoprene mixing ratio (5.9 ppbv 90th percentile value) was associated with deciduous forests and the largest monoterpene value was observed over evergreen forests (0.42 ppbv 90th percentile value). Observed mixing ratios scaled predictably with published emission factors, especially for deciduous forests, evergreen forests, shrubs, and croplands [Guenther *et al.*, 1995]. For example, isoprene emission rates of 372, 103, and 24 Tg C yr^{-1} qualitatively agree with observations of 1.77, 1.20, and 0.32 ppbv. Agricultural lands are noted to have suppressed emissions of both isoprene and monoterpenes as expected. The largest CO mixing ratios in the region (not shown in Figure 8) were observed in developed areas and croplands (200 and 204 ppbv 90th percentile value, respectively), compared to 174 ppbv in evergreen forest regions. Thus, since gas phase tracer mixing ratios differ between each land use type as predicted by literature emission rates, we assume that observed FBAP concentrations and properties can also be linked to land-type emission strength variability.

Bioaerosol characteristics illustrated by the box plot analysis in Figure 8 are contrasted below for each land cover type. Variability between land use types was small suggesting that emissions in the SEUS were generally homogeneous, i.e., the N_{FBAP} values for each land use type overlap in Figure 8. Still, the small differences

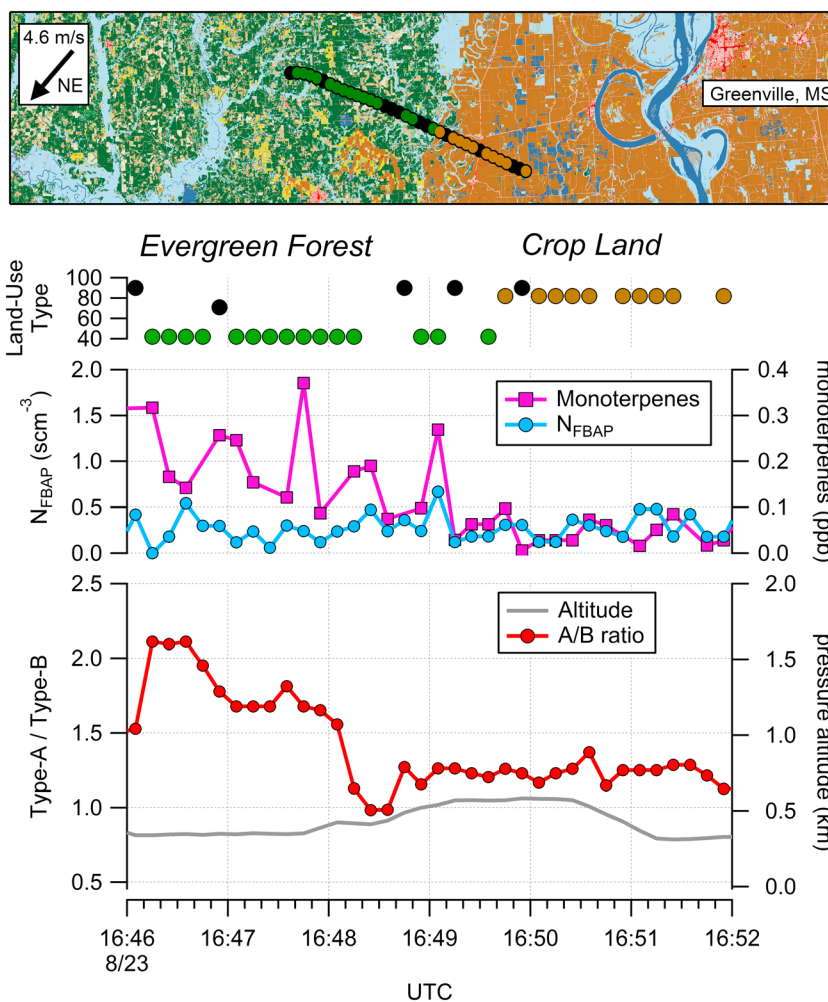


Figure 7. Example of sampling during a low-level leg in southeastern Arkansas. The transition from evergreen forest (green) to crop lands (brown) is illustrated on the NLCD2011 model (top) where land use ID = 42 denotes evergreen forest and land use ID = 82 denotes crop lands. Monoterpene mixing ratio, N_{FBAP} , Type A/Type B, and pressure altitude are plotted. The urban center of Greenville, MS, is shown just east of the Mississippi River (colored red on the NLCD2011 map).

between mean N_{FBAP} values for many of the land use types are statistically different, e.g., deciduous (0.34 scm^{-3}) and evergreen (0.25 scm^{-3}) forests are statistically significant at 95% confidence. Croplands, the only anthropogenically influenced land type assessed here, showed the highest mean N_{FBAP} (0.43 scm^{-3}). This mean value was statistically different from each other land use type except grasslands at 95% confidence. Still, we emphasize that the mean N_{FBAP} values for many of the other land use types are not statistically different due to either limitations in the method or similarities in real emissions.

The following sections describe differences in FBAP concentrations between land use types. Note that these comparisons are limited to measurements by UV-APS and WIBS instruments for consistency. Many other studies report concentrations in terms of culturable cells, but comparing these measurements with fluorescence-derived data is not necessarily valid. For comparisons, ground-level concentrations are approximately equivalent to N_{FBAP} reported here in units of scm^{-3} .

3.2.1. Forests

Forested lands cover 44% of the SEUS sampling region. FBAP concentrations over deciduous forests were greater than evergreen forests (Figure 8, bottom). Median N_{FBAP} from deciduous and evergreen forests was 0.31 and 0.24 scm^{-3} , respectively, and 90th/10th percentile values of $0.61/0.12$ and $0.47/0.06 \text{ scm}^{-3}$. Deciduous forests were also a slightly larger source of bioaerosol than evergreens on a relative basis as f_{FBAP} values were 9.4 and 8.3%, respectively.

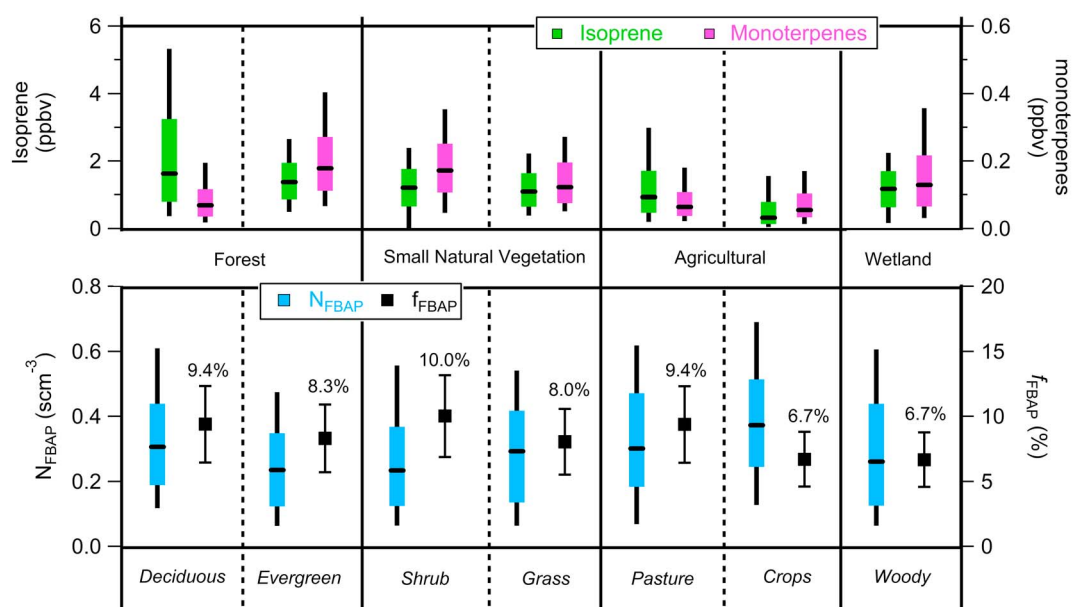


Figure 8. Campaign statistics for gas phase tracers (top, isoprene and monoterpenes) and (bottom) $N_{\text{FBAP}}/f_{\text{FBAP}}$ are shown for the SEUS land types. Box and whisker values are shown for interquartile and interdecile values as in Figure 5a. Square symbols represent the calculated f_{FBAP} value for each land cover type with error bars representing the calculated uncertainty. Data are segregated by forests, natural vegetation, agricultural regions, and wetlands.

Forests are a well-established source of bioaerosols. They contain significant leafy surface area to support bacterial communities and provide a smaller contribution from soils [Burrows *et al.*, 2009a, 2009b]. Exact emission mechanisms can be conflicting, with literature highlighting both understory and canopy sources. Gabey *et al.* [2010] reported much higher concentrations ($1\text{--}2.5\text{ cm}^{-3}$) from the forest understory of a Malaysian rainforest, with concentrations above the canopy ($0.05\text{--}0.1\text{ cm}^{-3}$) consistent with our airborne observations. Evergreen forest FBAP observations from Crawford *et al.* [2014] ranged from 0.05 to 0.3 cm^{-3} but had sources at the canopy level that exceeded concentrations at the ground.

3.2.2. Small Natural Vegetation

Natural vegetation, segregated as shrubs and grasslands, covers only a minor fraction (9%) of the SEUS region but has been identified as a source of airborne bacteria previously [Lighthart and Shaffer, 1995]. N_{FBAP} concentrations were generally lower from these sources than from deciduous forests. N_{FBAP} was higher for grasses than shrubs (median values of 0.29 and 0.23 cm^{-3} , respectively) but with similar interdecile ranges. f_{FBAP} for shrubs was highest for all SEUS sampling (10.0%), suggesting a lack of other coarse-mode aerosol sources here.

3.2.3. Agricultural Lands

Agricultural lands represent 28% of the SEUS land area. The largest FBAP concentrations in the region were observed over croplands, with a median value of 0.37 cm^{-3} and 90th/10th percentile values of $0.69/0.13\text{ cm}^{-3}$. Croplands differed from forest and vegetative lands as their relative contribution of FBAP was low (6.7%), suggesting that mineral dust emissions lacking fluorescence are also significant from these areas. Higher CO mixing ratios indicate that these coarse-mode particles are likely attributed to tilling or harvesting machinery. Bioaerosols can result from a multitude of agricultural processes beyond mechanical agitation during harvest, including animal confinement and composting, e.g., Adhikari *et al.* [2004], O'Connor *et al.* [2013], and Lee and Liao [2014].

3.2.4. Wetlands

Wetlands are another minor component of the SEUS region with approximately 8% of the land cover. Woody wetlands are specifically assessed here, as herbaceous wetlands were only sparsely sampled. While the absolute N_{FBAP} values have a similar median and range as other sources (0.26 cm^{-3} and $0.61/0.06\text{ cm}^{-3}$, respectively), f_{FBAP} values were as low as croplands (6.7%), suggesting that the freshwater wetlands may also be a source of nonfluorescing inorganic particles [Slade *et al.*, 2010].

3.3. Comparison of Land Cover Types

3.3.1. Model Flux Parameterization

Modeling studies have often employed an ecosystem-dependent concentration parameterization by *Burrows et al.* [2009a, 2009b] to represent bacterial fluxes from similar continental land cover types as compared here [e.g., *Spracklen and Heald* [2014]]. Global simulations indicate that bacteria and fungal spores have similar surface concentrations (both approximately $2.5 \times 10^4 \text{ m}^{-3}$ [*Spracklen and Heald*, 2014]), and our observed particle size in the 1–3 μm diameter range is consistent with the size of both bacteria and fungal spores [*Després et al.*, 2012; *Healy et al.*, 2012]. Thus, comparison with this parameterization serves to both put our FBAP observations in a modeling context and indicate regions potentially more affected by either bioaerosol type.

The *Burrows et al.* [2009a, 2009b] bacteria scheme suggests large concentration gradients should be observed between land types since emission fluxes vary considerably (Table 1): $1578 \text{ m}^{-2} \text{ s}^{-1}$ for crops, $187 \text{ m}^{-2} \text{ s}^{-1}$ for forests, $1811 \text{ m}^{-2} \text{ s}^{-1}$ for grasslands, and $619 \text{ m}^{-2} \text{ s}^{-1}$ for shrubs. Bacterial concentrations can be computed from these emission rates by assuming a BL height of 1.2 km [*Wagner et al.*, 2015] and a lifetime of 1–3 days. Thus, the published emission flux for crops ($1578 \text{ m}^{-2} \text{ s}^{-1}$) results in a BL concentration of $0.11\text{--}0.34 \text{ cm}^{-3}$, which is in good agreement with the observed median of 0.37 scm^{-3} and favors the longer (3 day) lifetime. Likewise, grasslands observations agree well with this model parameterization; flux-calculated concentrations of $0.13\text{--}0.39 \text{ cm}^{-3}$ compared to 0.29 scm^{-3} are observed.

The smaller bacterial fluxes used to represent forest ecosystems ($187 \text{ m}^{-2} \text{ s}^{-1}$) yield concentrations of $0.014\text{--}0.04 \text{ cm}^{-3}$ that underparameterize measured concentrations (0.31 scm^{-3} , for deciduous forests) by nearly an order of magnitude. Shrubs are similarly underrepresented but to a lesser extent ($0.04\text{--}0.13 \text{ cm}^{-3}$ from flux calculations compared to 0.23 scm^{-3} observed). Analogously, emissions fluxes of $1400 \text{ m}^{-2} \text{ s}^{-1}$ and $1200 \text{ m}^{-2} \text{ s}^{-1}$ are needed to support observed N_{FBAP} for pastures and wetlands, respectively; these types are not currently noted in the *Burrows et al.* [2009a, 2009b] scheme. The back-of-the-envelope calculations summarized here and in Table 1 are encouraging and generally agree well with our observations. The deviations noted for forest and shrub ecosystems likely suggest a significant contribution of fungal spores in these regions.

3.3.2. Spectral Fingerprinting

Since WIBS can potentially segregate FBAP types using a two-wavelength excitation and multidetector emission scheme (e.g., example in Figure 7), the utility of a spectral fingerprinting technique was explored similar to that used for source apportionment by other chemical techniques [*Decesari et al.*, 2007]. While Figure 7 exemplifies an ideal land type transition with an obvious shift in fluorescence signature, most transitions were less distinct. Thus, Figure 9 presents a summary of the aggregated WIBS fluorescence typing as a function of each of the land use types. Spectral results are shown as channel ratios, therefore making the results independent of concentration and applicable to other WIBS observations. Ratios are calculated from the number of particles fluorescing in each respective channel. For the example time series presented in Figure 7, a clear change in the Type A/Type B ratio is observed when transitioning from evergreen forest sampling to crop lands. These land cover types represent extremes in observed WIBS spectral variability in Figure 9.

Each of the different land use types fall on a spectral continuum based on the emission wavelength dependence using Type A/Type B and excitation wavelength dependence using Type C/Type B (Figure 9a) or Type BC/Type B (Figure 9b). Emissions from the evergreen forest and grasslands lie at one end of continuum, with large relative contributions from 310 to 400 nm band fluorescence and from 280 nm excitation (Type A). Crops and deciduous forests lie at the opposite end of the continuum, with a relatively larger contribution from 420 to 650 nm band fluorescence and 280 nm excitation (Type B). Each of the other land cover sources, including developed lands, has a spectral dependence between these extremes. Using the modified channel metric for excitation wavelength dependence (Figure 8b, Type BC) leads to further separation of land use types; pastures and shrubs may be segregated in Figure 9b but not in Figure 9a (using only the Type C channel). Statistics are generally not robust enough to completely separate different land types, and more work is necessary to understand the biological speciation underpinning these relationships. Still, based on intrinsic fluorescence properties, this analysis suggests that different species contribute to the FBAP populations emitted from these diverse sources.

3.4. Vertical Profiles and Transport Efficiency

Average vertical profiles of N_{FBAP} and f_{FBAP} for the SEUS are shown in Figure 10. N_{FBAP} is highest at low altitude and generally decreases with height since the major source of biological particles in the SEUS is the local

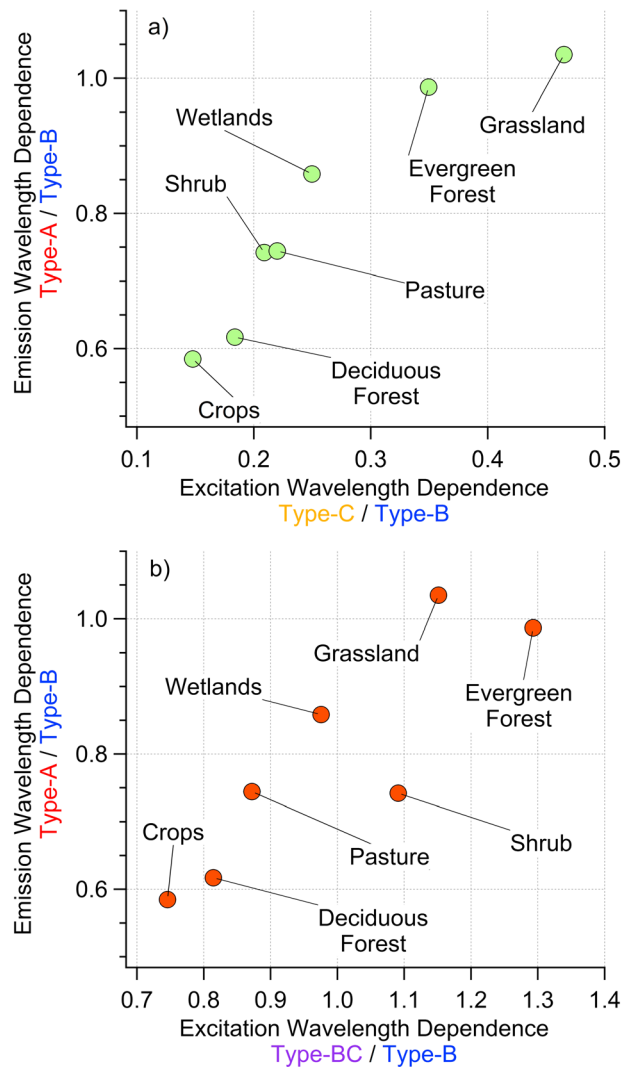


Figure 9. Segregation of land cover types using WIBS fluorescence signals for all low-altitude SEUS sampling. (a) The Type A/Type B ratio indicates an emission wavelength dependence (y axes), (b) while Type C/Type B (x axis) and Type BC/Type B (x axis) represent an excitation wavelength dependence. Single-particle events for each labeled land cover type are summed for each fluorescence signal, and the resulting ratios are calculated from these sums.

using measured CO mixing ratio (similar to the method used in Wagner *et al.* [2015]). The dilution ratio (DR) and VTE are calculated at each 0.5 km altitude step (*i*) in equations (2) and (3):

$$\text{Dilution Ratio (DR)}_i = \frac{\Delta X_i}{\Delta \text{CO}} = \frac{\bar{X}_i - X_{\text{background}}}{\bar{\text{CO}}_i - \text{CO}_{\text{background}}} \quad (2)$$

$$\text{Vertical Transport Efficiency (VTE)}_i = \frac{\text{DR}_i}{\text{DR}_{\text{alt} < 0.5 \text{ km}}}, \quad (3)$$

where *X* represents any measurement, \bar{X} and $\bar{\text{CO}}$ are average values, $X_{\text{background}}$ and $\text{CO}_{\text{background}}$ are background values based on the 5th percentile value at 6–12 km altitude for each parameter, respectively. Transport efficiency is then the ratio of the DR at each altitude step with the DR at the lowest altitude. By definition, the VTE for the lowest altitude is unity. This method assumes all FBAP are emitted at the surface and that horizontal transport into and out of the region as a whole is negligible. Thus, we limit this analysis

planetary BL. Average surface level (less than 0.5 km) N_{FBAP} was $0.34 \pm 0.25 \text{ scm}^{-3}$, which decreases to $0.07 \pm 0.12 \text{ scm}^{-3}$ at 3 km and $0.018 \pm 0.058 \text{ scm}^{-3}$ at 6 km altitude. Moderate convective lofting in the region [Siebesma, 1998] is the likely source of midaltitude FBAP, which by assuming there is no significant entrainment from aloft transports approximately one third of the bioaerosol concentration out of the BL. Despite low concentrations in the FT, N_{FBAP} exhibited vertical structure with a secondary maxima at 8–8.5 km ($0.012 \pm 0.046 \text{ scm}^{-3}$) and at 10–10.5 km altitude ($0.020 \pm 0.098 \text{ scm}^{-3}$).

In the SEUS at this time, Wagner *et al.* [2015] quantified an average BL height of 1.2 km with a transition layer between 1.5 and 3.0 km. This vertical structure is consistent with SEUS simulations presented in Kim *et al.* [2012] that define typical fair weather cloud bottoms and tops at 1.2 and 2.7 km, respectively. WIBS measurements suggest that 49% of the column FBAP number concentration was observed in this BL, but a significant fraction (28%) is lofted into the transition (cloud) layer and above (9.5%). Presumably, this lofted FBAP is able to be transported horizontally outside of the SEUS more efficiently and potentially acts as INP in the upper troposphere upon further synoptic scale uplift.

To quantify vertical FBAP transport by BL venting and through fair weather shallow convection more rigorously, a vertical transport efficiency (VTE) term was computed as the ratio of ground-level FBAP concentration to concentrations at altitude, explicitly correcting for dilution

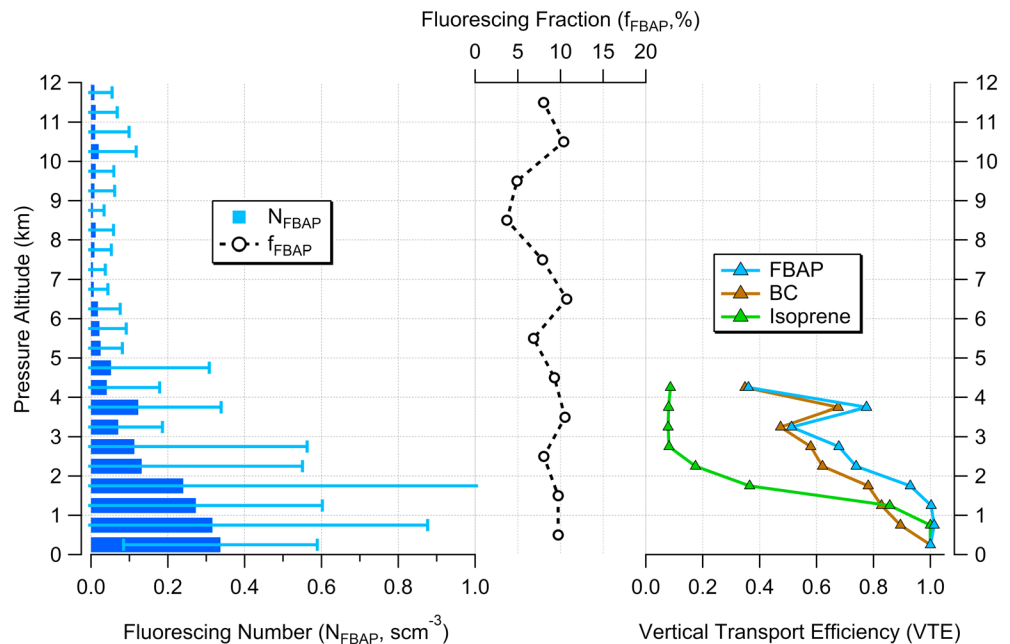


Figure 10. Average full-campaign vertical profiles from the SEUS region for (left) N_{FBAP} , (middle) f_{FBAP} , and (right) vertical transport efficiency. Error bars represent the average $N_{\text{FBAP}} \pm 1$ standard deviation. Transport efficiency is defined in equations (2) and (3) in the text.

to altitudes below 4.5 km where aerosol measurements are more likely linked to local emissions and local convective transport. Above this height, air masses are expected to be decoupled from the surface and are a result of long-range transport. VTE values are calculated for FBAP, BC aerosol, and isoprene in Figure 10 (right).

FBAP has a VTE of unity through the lowest 1.5 km, consistent with the *Wagner et al.* [2015] height of 1.2 km and for the well-mixed SEUS BL. FBAP VTE values decrease with height above the BL to an average value of 0.36 at 4.5 km. Since VTE generally decreases with height, the anomalously large VTE values for both FBAP and black carbon (BC) just below the nominal freezing level at 4.0 km (FBAP VTE = 0.78) may be due to efficient detrainment at the neutral buoyancy level near cloud top height, which extended to approximately 3.0 km in the region [*Wagner et al.*, 2015]. VTE values of between 0.93 and 0.51 at 1.75 and 3.25 km altitude highlight the relatively efficient transport of FBAP out of the planetary BL in the SEUS.

For comparison, isoprene's short lifetime (less than 3 h) manifests as a VTE that quickly decreases above the surface to 0.08 above 2.5 km altitude, transport that is more than 5 times less efficient than FBAP. This serves as both a proof of concept for the VTE calculation and gives context to the time scale of FBAP lofting. The VTE for BC aerosol mass concentration also remarkably decreases faster than FBAP with increasing altitude throughout the column. Just above the BL at 1.75 km, VTE for FBAP (0.93) is 19% greater than VTE for BC (0.78). Since both FBAP and BC are primarily emitted at the surface and have been implicated as good ice nuclei INP, these results show that the shallow convective lofting of FBAP is at least equal to, if not more efficient than for BC. This observation of highly efficient vertical transport should help to highlight the potential importance of bioaerosol as a regionally relevant INP, and that these particles survive vertical transport despite their larger size.

Mineral dust aerosol is also a well-studied INP, but the VTE of these nonfluorescing particles was not significantly different from FBAP. Likewise, f_{FBAP} was constant throughout the atmospheric column with no distinct vertical trend. Values of f_{FBAP} ranged from 8.0 to 10.7% below 4.5 km altitude, suggesting that lofting processes (i.e., convective uplift, IN activation) are not biased toward (or against) the biological content of the population. Deviations of f_{FBAP} as low as 3.7% aloft are likely the result of long-range transport of air masses with larger mineral dust significance. A comparison of modeled and observed global cirrus supersaturations indicates that 1–10% of coarse aerosol act as INP [*Wang et al.*, 2014], a result that qualitatively (or coincidentally) suggests that bioaerosols play a significant role in cirrus formation based on the observed 3.7–10.7% f_{FBAP} range reported here.

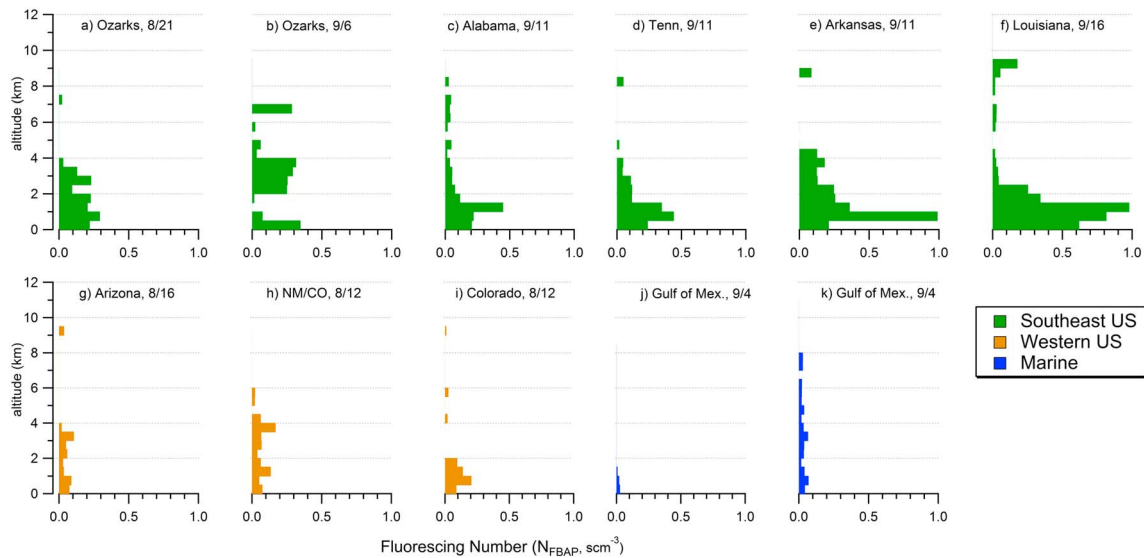


Figure 11. Vertical profiles for individual spiral or ascent/descent maneuvers in (a–f) SEUS, (g–i) western U.S., and (j and k) marine regions.

3.5. Context of SEUS Sampling: Comparison to Other North American Sources

Finally, although statistics are poor for sampling other regions in North America during SEAC⁴RS, it is useful to put SEUS profiles in context with measurements in the western U.S. and over the marine environment (i.e., the Gulf of Mexico). Profile locations are mapped in Figure 1. Figure 11 shows six individual profiles representative of the SEUS region (a–f), along with three in the western U.S. (g–i) and two over the Gulf of Mexico (j and k). Individual SEUS profiles are consistent with the average profile shown in Figure 10; highest concentrations are at low altitude and smaller concentrations were observed in the entrainment layer and FT. Midaltitude concentrations are always elevated above the free tropospheric background to some extent, with profiles over the Ozarks (6 September, Figure 11b) and Arkansas (11 September, Figure 11e) characterized by especially distinct lofted bioaerosol concentrations. Fairly good regional agreement was observed for three profiles obtained on a single day (11 September), illustrating some degree of spatial homogeneity in the region on a single day. Comparing these SEUS profiles to western U.S. and marine regions, it is clear that not only are BL emissions dominant in the SEUS, but this manifests as much higher lofted concentrations (2–5 km altitude) compared to near-zero concentrations at this altitude in other regions.

SEUS f_{FBAP} measurements are compared to other FBAP sources using a frequency histogram in Figure 12. Values of f_{FBAP} in the SEUS covered a range of more than 3 orders of magnitude from roughly 0.06 to 50%, with the majority of measurements falling in the 1–40% range with an average of 8.5%. Marine sampling yielded very low f_{FBAP} values near the surface (0.73%) indicating that, relatively, an order of magnitude fewer particles containing biological material are emitted from the Gulf of Mexico in the late summer.

An unexpected aspect of the SEAC⁴RS mission was a strong incursion of transported Saharan Air Layer (SAL) mineral dust on 8 August that served as a comparative null case for FBAP detection. NAAPS (Navy Aerosol Analysis and Prediction System) [Christensen, 1997] modeling forecasts and Hybrid Single-Particle Lagrangian Integrated Trajectory (HYSPLIT) [Draxler and Rolph, 1997] back trajectory analysis confirmed the African source region. Very high dust concentrations (250 scm^{-3} measured by the WIBS and greater than 100Mm^{-1} extinction coefficient) were observed up to approximately 3 km altitude just off the Louisiana coast during the event. These low particle number concentrations and vertical extent were remarkably similar to observations made during the NAMMA (NASA African Monsoon Multidisciplinary Analysis) campaign that explicitly targeted SAL dust during trans-Atlantic transport [Chen et al., 2011], suggesting that very little mixing with continental air had occurred. Only a small fraction (0.17%) of the SAL dust particles contained a biological component, an f_{FBAP} value that was the lowest observed during SEAC⁴RS. Other studies have found similarly low fractional contribution for long-range transported dust (e.g., 0.2% for Asian dust [Hallar et al., 2011]), suggesting that on a relative basis (1) mineral dusts are predominantly nonbiological compared to SEUS emissions, and (2)

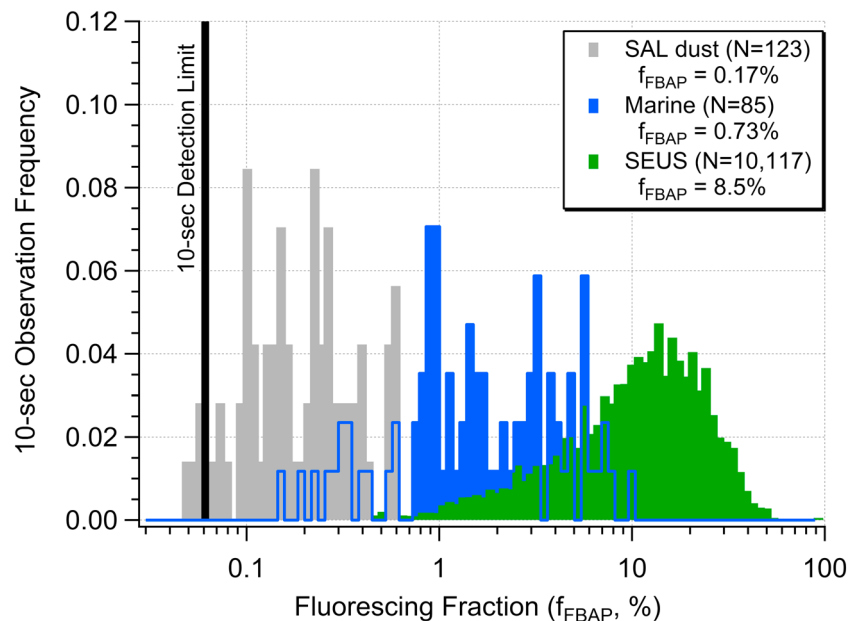


Figure 12. Summary histogram of fluorescing-fraction (f_{FBAP}) observations during SEAC⁴RS. Values for Saharan air layer (SAL) dust aerosols (gray), marine aerosols (blue), and SEUS (green) are shown. The approximate WIBS 10 s detection limit for f_{FBAP} (0.061%) is plotted as a black line for context. The number of 10 s samples (N) and average f_{FBAP} value for each source is noted in the legend. SAL dust was identified based on NAAPS model run for 18Z on 8 August 2013 predicting 80–160 $\mu\text{g m}^{-3}$ of dust at the surface over southern Texas and Louisiana. HYSPLIT back trajectories were initiated at 20Z at 500, 1000, and 2000 m heights using Global Data Assimilation System meteorological data and model vertical velocity, each originating over western Africa within 20 days.

mineral dusts were at most a minor interference to FBAP WIBS detection (i.e., mineral dust sample did not significantly fluoresce) in the SEUS.

4. Conclusions

A WIBS-4A was modified for airborne operation and deployed aboard the NASA DC-8 aircraft during SEAC⁴RS. Low-altitude FBAP number concentrations (N_{FBAP}) for the SEUS region were observed in the 0.1–0.43 scm^{-3} range, highest during dry periods with either low or high wind speed.

A land use model was used to explain spatial variability of low-altitude bioaerosol properties throughout the SEUS, with the highest N_{FBAP} observed over agricultural croplands (0.37 scm^{-3}) and lowest concentrations associated with evergreen forests (0.24 scm^{-3}). Fluorescence and size distribution characteristics showed a distinct difference between evergreen and deciduous forests and between croplands and grasslands, and the spectral fingerprinting analysis presented here may be applied to future measurements providing a method to source-apportion FBAP after long-range transport. A comparison of measured concentrations to model emission fluxes showed excellent agreement for N_{FBAP} from grasslands and crops, while shrubs and forests were significantly underparameterized (by a factor of 2 and 10, respectively). Increasing the modeled emission fluxes of forests, especially, may have significant ramifications on global INP concentrations and potentially reemphasize the climate relevance of bioaerosols on a global scale.

Vertical profile measurements throughout the SEUS were used to assess the vertical transport efficiency of coarse-mode FBAP (geometric mode of 2.1 μm) out of the concentrated planetary BL. After accounting for dilution and background concentrations, approximately 40% of ground-level N_{FBAP} was lofted out of the planetary boundary layer due most likely to shallow convection in the region, a transport pathway that is at least equally efficient as for BC aerosol.

Quantifying FBAP using the Type ABC particles was done based on balancing potential positive bias of nonbiological material and negative bias from biological material that does not show fluorescence in all

WIBS channels. For example, our Type ABC definition results in an average low-altitude FBAP concentration of 0.34 scm^{-3} in the SEAC⁴RS study region. Employing the two-channel definition used by Gabey *et al.* [2010] would result in a concentration of 0.63 scm^{-3} for the same data set, and 0.99 scm^{-3} by defining FBAP as fluorescing in any one of the WIBS channels as in Perring *et al.* [2015], although this higher concentration would be partially offset by higher fluorescence detector thresholds. This range of a factor of 3 in FBAP concentration certainly points toward needing more work to better understand the intrinsic fluorescence of different species and typical atmospheric interferants. For example, the reported WIBS-based number concentrations here are generally higher than those reported by Perring *et al.* [2015] for the SEUS region ($0.02\text{--}0.09 \text{ cm}^{-3}$), but with similar fractions and size distributions. Clearly more rigorous intercomparison of FBAP measurement techniques, including both fluorescence and mass spectrometry methods, is needed in the future to begin to more systematically constrain ground-level emissions, the source apportionment of FBAP, and the efficiency and mechanisms associated with convective transport.

Acknowledgments

This research was funded by NASA's Upper Atmosphere Research Program, Radiation Sciences Program, and Tropospheric Chemistry Program. We would like to thank Gary Granger at Droplet Measurement Techniques for technical support. We wish to thank the pilots and flight crews of NASA's DC-8 aircraft for their important support, as well as the SEAC⁴RS science team for supporting data and discussion. We especially thank NASA for funding to procure the WIBS instrument through the Science Innovation Fund at Langley Research Center. We would also like to acknowledge helpful comments during the peer-review process. Please contact the corresponding author to request data at luke.ziamba@nasa.gov.

References

- Adhikari, A., M. M. Sen, S. Gupta-Bhattacharya, and S. Chanda (2004), Volumetric assessment of airborne fungi in two sections of a rural indoor dairy cattle shed, *Environ. Int.*, *29*(8), 1071–1078.
- Anderson, J. R., E. E. Hardy, J. T. Roach, and R. E. Witmer (1976), A land use and land cover classification system for use with remote sensor data, *U.S. Geol. Surv. Prof. Pap.*, *964*.
- Burrows, S. M., W. Elbert, M. G. Lawrence, and U. Pöschl (2009a), Bacteria in the global atmosphere—Part 1: Review and synthesis of literature data for different ecosystems, *Atmos. Chem. Phys.*, *9*(23), 9263–9280.
- Burrows, S. M., T. Butler, P. Jöckel, H. Tost, A. Kerckweg, U. Pöschl, and M. G. Lawrence (2009b), Bacteria in the global atmosphere—Part 2: Modeling of emissions and transport between different ecosystems, *Atmos. Chem. Phys.*, *9*(23), 9281–9297.
- Chen, G., *et al.* (2011), Observations of Saharan dust microphysical and optical properties from the Eastern Atlantic during NAAMA airborne field campaign, *Atmos. Chem. Phys.*, *11*, 723–740.
- Christensen, J. H. (1997), The Danish Eulerian hemispheric model—A three-dimensional air pollution model used for the Arctic, *Atmos. Environ.*, *31*, 4169–4191.
- Clarke, A. D., Y. Shinozuka, V. N. Kapustin, S. Howell, B. Huebert, S. Doherty, and K. G. Moore (2004), Size distributions and mixtures of dust and black carbon aerosol in Asian outflow: Physiochemistry and optical properties, *J. Geophys. Res.*, *109*, D15S09, doi:10.1029/2003JD004378.
- Crawford, I., N. H. Robinson, M. J. Flynn, V. E. Foot, M. W. Gallagher, J. A. Huffman, W. R. Stanley, and P. H. Kaye (2014), Characterisation of bioaerosol emissions from a Colorado pine forest: Results from the BEACHON-RoMBAS experiment, *Atmos. Chem. Phys.*, *8559*–*8578*.
- Creamean, J. M., K. J. Suski, D. Rosenfeld, A. Cazorla, P. J. DeMott, R. C. Sullivan, and J. M. Tomlinson (2013), Dust and biological aerosols from the Sahara and Asia influence precipitation in the western US, *Science*, *339*(6127), 1572–1578.
- Cziczo, D. J., K. D. Froyd, C. Hoose, E. J. Jensen, M. Diao, M. A. Zondlo, and D. M. Murphy (2013), Clarifying the dominant sources and mechanisms of cirrus cloud formation, *Science*, *340*(6138), 1320–1324.
- Decesari, S., M. Mircea, F. Cavalli, S. Fuzzi, F. Moretti, E. Tagliavini, and M. C. Facchini (2007), Source attribution of water-soluble organic aerosol by nuclear magnetic resonance spectroscopy, *Environ. Sci. Technol.*, *41*(7), 2479–2484.
- DeMott, P. J., A. J. Prenni, X. Liu, S. M. Kreidenweis, M. D. Petters, C. H. Twohy, and D. C. Rogers (2010), Predicting global atmospheric ice nuclei distributions and their impacts on climate, *Proc. Natl. Acad. Sci. U.S.A.*, *107*(25), 11,217–11,222.
- DeMott, P. J., *et al.* (2011), Resurgence in ice nuclei measurement research, *Bull. Am. Meteorol. Soc.*, *92*(12), 1623–1635.
- Després, V. R., J. A. Huffman, S. M. Burrows, C. Hoose, A. S. Safatov, G. Buryak, and R. Jaenicke (2012), Primary biological aerosol particles in the atmosphere: A review, *Tellus B*, *64*, doi:10.3402/tellusb.v64i0.15598.
- Draxler, R. R., and G. D. Rolph (1997), HYSPLIT (HYbrid Single-Particle Lagrangian Integrated Trajectory) Model, NOAA Air Resour. Lab., College Park, Md. [Available at NOAA ARL READY Website <http://www.arl.noaa.gov/HYSPLIT.php>.]
- Ervens, B., B. J. Turpin, and R. J. Weber (2011), Secondary organic aerosol formation in cloud droplets and aqueous particles (aqSOA): A review of laboratory, field and model studies, *Atmos. Chem. Phys.*, *11*(21), 11,069–11,102.
- Gabey, A. M., M. W. Gallagher, J. Whitehead, J. R. Dorsey, P. H. Kaye, and W. R. Stanley (2010), Measurements and comparison of primary biological aerosol above and below a tropical forest canopy using a dual channel fluorescence spectrometer, *Atmos. Chem. Phys.*, *10*(10), 4453–4466.
- Guenther, A., P. Zimmerman, and M. Wildermuth (1994), Natural volatile organic compound emission rate estimates for US woodland landscapes, *Atmos. Environ.*, *28*(6), 1197–1210.
- Guenther, A., *et al.* (1995), A global model of natural volatile organic compound emissions, *J. Geophys. Res.*, *100*, 8873–8892, doi:10.1029/94JD02950.
- Hallar, A., G. Chirokova, I. McCubbin, T. H. Painter, C. Wiedinmyer, and C. Dodson (2011), Atmospheric bioaerosols transported via dust storms in the western United States, *Geophys. Res. Lett.*, *38*, L17801, doi:10.1029/2011GL048166.
- Heald, C. L., and D. V. Spracklen (2009), Atmospheric budget of primary biological aerosol particles from fungal spores, *Geophys. Res. Lett.*, *36*, L09806, doi:10.1029/2009GL037493.
- Healy, D. A., D. J. O'Connor, A. M. Burke, and J. R. Sodeau (2012), A laboratory assessment of the Waveband Integrated Bioaerosol Sensor (WIBS-4) using individual samples of pollen and fungal spore material, *Atmos. Environ.*, *60*, 534–543.
- Hoose, C., and O. Mohler (2012), Heterogeneous ice nucleation on atmospheric aerosols: A review of results from laboratory experiments, *Atmos. Chem. Phys.*, *12*, 12,531–12,621.
- Hoose, C., J. E. Kristjánsson, and S. M. Burrows (2010), How important is biological ice nucleation in clouds on a global scale?, *Environ. Res. Lett.*, *5*(2), 024009, doi:10.1088/1748-9326/5/2/024009.
- Huffman, J. A., B. Treutlein, and U. Pöschl (2010), Fluorescent biological aerosol particle concentrations and size distributions measured with an Ultraviolet Aerodynamic Particle Sizer (UV-APS) in central Europe, *Atmos. Chem. Phys.*, *10*(7), 3215–3233.
- Huffman, J. A., A. J. Prenni, P. J. DeMott, C. Pöhlker, R. H. Mason, N. H. Robinson, and D. J. Gochis (2013), High concentrations of biological aerosol particles and ice nuclei during and after rain, *Atmos. Chem. Phys.*, *13*(13), 6151–6164.
- Jaenicke, R. (2005), Abundance of cellular material and protein in the atmosphere, *Science*, *308*(5718), 73–73.

- Jin, S., L. Yang, P. Danielson, C. Homer, J. Fry, and G. Xian (2013), A comprehensive change detection method for updating the National Land Cover Database to circa 2011, *Remote Sens. Environ.*, *132*, 159–175.
- Jones, A. M., and R. M. Harrison (2004), The effects of meteorological factors on atmospheric bioaerosol concentrations—A review, *Sci. Total Environ.*, *326*(1), 151–180.
- Kaye, P. H., J. E. Barton, E. Hirst, and J. M. Clark (2000), Simultaneous light scattering and intrinsic fluorescence measurement for the classification of airborne particles, *Appl. Optics*, *39*(21), 3738–3745.
- Kaye, P., W. R. Stanley, E. Hirst, E. V. Foot, K. L. Baxter, and S. J. Barrington (2005), Single particle multichannel bio-aerosol fluorescence sensor, *Opt. Express*, *13*(10), 3583–3593.
- Kim, S. W., M. C. Barth, and M. Trainer (2012), Influence of fair-weather cumulus clouds on isoprene chemistry, *J. Geophys. Res.*, *117*, D10302, doi:10.1029/2011JD017099.
- Lawson, R. P. (2011), Effects of ice particles shattering on optical cloud particle probes, *Atmos. Meas. Tech.*, *4*, 939–968.
- Lee, S. A., and C. H. Liao (2014), Size-selective assessment of agricultural workers' personal exposure to airborne fungi and fungal fragments, *Sci. Total Environ.*, *466*, 725–732.
- Lighthart, B., and B. T. Shaffer (1995), Viable bacterial aerosol particle size distributions in the midsummer atmosphere at an isolated location in the high desert chaparral, *Aerobiologia*, *11*(1), 19–25.
- McNaughton, C. S., A. D. Clarke, S. G. Howell, M. Pinkerton, B. Anderson, K. L. Thornhill, and H. Maring (2007), Results from the DC-8 Inlet Characterization Experiment (DICE): Airborne versus surface sampling of mineral dust and sea salt aerosols, *Aerosol Sci. Technol.*, *41*(2), 136–159.
- Müller, M., T. Mikoviny, S. Feil, S. Haidacher, G. Hanel, E. Hartungen, and P. Sulzer (2014), A compact PTR-ToF-MS instrument for airborne measurements of VOCs at high spatio-temporal resolution, *Atmos. Meas. Tech.*, *7*, 5533–5558.
- O'Connor, D. J., D. A. Healy, and J. R. Sodeau (2013), The on-line detection of biological particle emissions from selected agricultural materials using the WIBS-4 (Waveband Integrated Bioaerosol Sensor) technique, *Atmos. Environ.*, *80*, 415–425.
- Pan, Y. L., S. C. Hill, R. G. Pinnick, J. M. House, R. C. Flagan, and R. K. Chang (2011), Dual-excitation-wavelength fluorescence spectra and elastic scattering for differentiation of single airborne pollen and fungal particles, *Atmos. Environ.*, *45*(8), 1555–1563.
- Perring, A. E., J. P. Schwarz, D. Baumgardner, M. T. Hernandez, D. V. Spracklen, C. L. Heald, and D. W. Fahey (2015), Airborne observations of regional variation in fluorescent aerosol across the United States, *J. Geophys. Res. Atmos.*, *120*, 1153–1170, doi:10.1002/2014JD022495.
- Pöhlker, C., J. A. Huffman, and U. Pöschl (2012), Autofluorescence of atmospheric bioaerosols—Fluorescent biomolecules and potential interferences, *Atmos. Meas. Tech.*, *5*(1), 37–71.
- Pratt, K. A., P. J. DeMott, J. R. French, Z. Wang, D. L. Westphal, A. J. Heymsfield, and K. A. Prather (2009), In situ detection of biological particles in cloud ice-crystals, *Nat. Geosci.*, *2*(6), 398–401.
- Prospero, J. M., E. Blades, G. Mathison, and R. Naidu (2005), Interhemispheric transport of viable fungi and bacteria from Africa to the Caribbean with soil dust, *Aerobiologia*, *21*(1), 1–19.
- Sachse, G. W., G. F. Hill, L. O. Wade, and M. G. Perry (1987), Fast-response, high-precision carbon monoxide sensor using a tunable diode laser absorption technique, *J. Geophys. Res.*, *92*, 2071–2081, doi:10.1029/JD092iD02p02071.
- Schwarz, J. P., et al. (2006), Single-particle measurements of midlatitude black carbon and light-scattering aerosols from the boundary layer to the lower stratosphere, *J. Geophys. Res.*, *111*, D16207, doi:10.1029/2006JD007076.
- Sesartic, A., U. Lohmann, and T. Storelvmo (2012), Bacteria in the ECHAM5-HAM global climate model, *Atmos. Chem. Phys.*, *12*(18), 8645–8661.
- Siebesma, A. P. (1998), *Shallow Cumulus Convection*. In *Buoyant Convection in Geophysical Flows*, pp. 441–486, Springer, Netherlands.
- Slade, J. H., T. M. VanReken, G. R. Mwaniki, S. Bertman, B. Stirn, and P. B. Shepson (2010), Aerosol production from the surface of the Great Lakes, *Geophys. Res. Lett.*, *37*, L18807, doi:10.1029/2010GL043852.
- Spracklen, D. V., and C. L. Heald (2014), The contribution of fungal spores and bacteria to regional and global aerosol number and ice nucleation immersion freezing rates, *Atmos. Chem. Phys.*, *14*, 9051–9059.
- Szymanski, W. W. (2002), Aerosol concentration measurement with multiple light scattering system and laser aerosol spectrometer, *Atmos. Res.*, *62*, 255–265.
- Tobo, Y., A. J. Prenni, P. J. DeMott, J. A. Huffman, C. S. McCluskey, G. Tian, and S. M. Kreidenweis (2013), Biological aerosol particles as a key determinant of ice nuclei populations in a forest ecosystem, *J. Geophys. Res. Atmos.*, *118*, 10,100–10,110, doi:10.1002/jgrd.50801.
- Wagner, N. L., C. A. Brock, W. M. Angevine, A. Beyersdorf, P. Campuzano-Jost, D. Day, and G. Huey (2015), In situ vertical profiles of aerosol extinction, mass, and composition over the southeast United States during SENEX and SEAC⁴RS: Observations of a modest aerosol enhancement aloft, *Atmos. Chem. Phys.*, *15*(3), 3127–3172.
- Wang, M., X. Liu, K. Zhang, and J. M. Comstock (2014), Aerosol effects on cirrus through ice nucleation in the Community Atmosphere Model CAM5 with a statistical cirrus scheme, *J. Adv. Model. Earth Syst.*, *6*(3), 756–776, doi:10.1002/2014MS000339.